Resources, Conservation & Recycling 178 (2022) 106038

Contents lists available at ScienceDirect

Resources, Conservation & Recycling

journal homepage: www.elsevier.com/locate/resconrec

Microstructure and durability performance of sustainable cementitious composites containing high-volume regenerative biosilica

Jiaqi Li [a], Qingxu Jin [b], Wenxin Zhang [a], Chen Li [a,c,*], Paulo J.M. Monteiro [a]

[a] Department of Civil and Environmental Engineering, University of California, Berkeley, CA 94720, USA
[b] Department of Civil and Environmental Engineering, Michigan State University, East Lansing, MI 48824, USA
[c] Key Laboratory of Advanced Civil Engineering Materials of Ministry of Education, School of Materials Science and Engineering, Tongji University, Shanghai, 201804, China

ARTICLE INFO

Keywords:
Biomass residue
Biosilica
Durability
Sustainability
Diatomite

ABSTRACT

To promote diatom-based biofuel productions in clean energy, this paper explores the potential of using biosilica as a renewable and regenerative byproduct from diatom-based biofuel production in cementitious materials. High-purity diatomite (DE), a biosilica model compound, is selected to investigate the microstructure and durability performance of diatom-based cementitious composites. The replacement of portland cement with 30 wt.% DE significantly enhances the resistance to leaching, reduces the rapid chloride permeability, but increases the drying shrinkage at early ages. The microstructure of DE-containing matrix is refined due to the lime-silica reaction, and the interfacial transition zone of DE-containing concrete is densified. Overall, the DE-induced microstructural changes enhance the durability performance of DE-containing cementitious composites, which in turn demonstrates the feasibility of using biosilica as a sustainable cement substitute. The use of biosilica from diatom-based biofuel production can potentially reduce the CO_2 emissions of carbon-intensive concrete production and promote the development of clean energy.

1. Introduction

The consumption of fossil fuels is the primary contributor to CO_2 emissions, an important greenhouse gas that is responsible for climate change. The pursuit of renewable energy has become one of the key solutions to mitigating climate change. The advancement in technology has fueled a drastic growth in renewable energy consumption, among which biomass has shown an annual growth of 8% for renewable electricity generation in 2019 (IEA 2020). Unlike conventional energy sources such as petroleum, coal, and natural gas, biomass-based energy such as biofuel is considered environmentally benign and potentially carbon-negative (Kim et al., 2020). Biofuel is the fuel that is derived from biomass, including plants, algae, and animal wastes (Rajkumar et al., 2014;Abdulkareem et al., 2019). Among these biomass sources, microalgae contain a high biomass yield per unit of light exposure and area (Rajkumar et al., 2014). Moreover, the microalgae-based biofuel provides additional environmental benefits since its production does not have fresh or arable land requirements (Rajkumar et al., 2014).

One of the viable sources for microalgae-based biofuel production are freshwater and marine diatoms (Graham et al., 2012;Levitan et al., 2014;Wang and Seibert, 2017;Ejaz et al., 2021). To further promote the environmental and capital advantages of biofuel production, the utilization of biomass residue is of great interest (Kim et al., 2020;Ho et al., 2014;Luhar et al., 2019;Alcaraz et al., 2019). With the exception of Didimosphenia geminate diatom that produces both silica and calcite (Ehrlich et al., 2016), the biomass residue of diatoms is chitin-containing biosilica (Brunner et al., 2009), which is structurally similar to diatomite (fossilized diatom, also termed as DE). Possessing an amorphous structure, diatom-like biosilica could be potentially used as a regenerative source of supplementary cementitious materials (SCMs) and help reduce the environmental impacts from portland cement (PC) production (Snellings et al., 2012). The DE that is reported in the majority of previous studies for the use of SCM has low amorphous biosilica content (<50 wt.%;Esen and Kurt, 2018;Choi et al., 2015;Degirmenci and Yilmaz, 2009;Kastis et al., 2006;Fragoulis et al., 2005;Rahhal and Talero, 2009), which unfortunately cannot be used as a model compound of biosilica from diatom-based biofuel productions. Additionally, the DE substitution level in these studies is typically limited to up to 20 wt.% of total binder content. Such low substitution level is due to the low amorphous silica content in the DE being used, which results in a low

* Corresponding author.
E-mail address: lichen_0712@tongji.edu.cn (C. Li).

https://doi.org/10.1016/j.resconrec.2021.106038
Received 12 June 2021; Received in revised form 10 October 2021; Accepted 4 November 2021
Available online 16 November 2021

reactivity with PC. These two limitations have rendered these studies with little improvement on material's strengths.

It is desirable to investigate DE with a higher amorphous biosilica content and higher cement replacements in cementitious composites, as well as to model the effects of diatom-based biofuel residue on the composites' microstructure and durability performance. Our recent study (Li et al., 2019) has successfully demonstrated that DE with 83+ wt.% biosilica content can replace up to 40 wt.% PC in mortar/concrete and significantly improves the composite's compressive strengths. The partial replacement of PC with high-quality DE could reduce the global warming potential by 50%, and PM10 and lead emissions from mortar/concrete production in addition to strength enhancements (Li et al., 2020). Due to the high surface area of biosilica, the use of high-quality DE as SCMs could lead to a high water-demand of DE-containing cementitious materials to maintain desirable workability, especially for the replacement level to 40 wt.% (Monteiro et al., 2019). The use of superplasticizer could compensate the high water-demand, but would inhibit the early age strength development and increase the materials' cost (Monteiro et al., 2019). Therefore, the optimal high-quality DE substitution level for PC is suggested to be 30 wt.% (Li et al., 2019), which will be adopted in this study as well.

Leveraging the improved strength, recent studies have focused on examining the durability performance of DE-containing cementitious composites (Wei et al., 2016;Xu et al., 2014). However, many contradictory results have been reported. For example, studies reported that the replacement of PC with DE in concrete decreased the chloride permeability (Gerengi et al., 2013) and resistance to corrosion (Tagnit-Hamou et al., 2003), while other studies showed that the replacement increased the chloride permeability (Papadakis et al., 2002), and resistance to corrosion (;Gerengil et al., 2017; Kurtay et al., 2020). Contradictory results regarding the effect of DE on drying shrinkage of mortar were also found in (Davis and Klein, 1950) and (South, 2009). All the aforementioned contradiction could be related to the lack of the characterization of DE since DE in these studies has different biosilica content and even contains a significant amount of calcite, crystalline silica (i.e. low reactivity), and/or other impurities (Pokorný et al., 2019;Kastis et al., 2006). Therefore, more systematical studies are needed to evaluate the durability performance of DE-containing cementitious composites, especially on the DE with high purity and substitution levels. To provide a better understanding on the mechanism, the microstructural properties and chemical evolutions of DE-containing cementitious composites should also be characterized.

This paper uses a DE with high biosilica content to replace up to 30% portland cement and aims to address the following questions to explore the mechanism of the durability performance of DE-containing cementitious composites: 1) How does biosilica affect leaching resistance of the composites? In particular, are the pores in DE, lowered Ca content in the matrix, and reduced pH by lime-silica (pozzolanic) reaction harmful for leaching resistance? 2) How does the microstructure of raw DE affect chloride (Cl^-) permeability? For instance, do the pores in DE behave as channels for Cl^- transport? 3) How does DE affect the composites' dimensional stability? Can the absorbed water in DE self-cure the concrete and hence limit its drying shrinkage? To address these questions, this study investigated the leaching resistance of hardened pastes by immersion in ammonium nitrate solution as the leaching agent. The Cl^- permeability of DE-containing concrete was investigated. The drying shrinkage of mortars was measured for up to 365 days. Moreover, to further explore the feasibility of using DE in commercial PC, which is often pre-blended with limestone (mainly calcite;Gruskovnjak et al., 2008), the effect of calcite on the durability of a PC-DE-calcite ternary cement system is also examined. With the information, we are able to establish the relationship between the microstructural and chemical properties and the durability performance of high-quality DE-containing cementitious composites. The results have great implications for the use of the byproduct from microalgae-based biofuel in the production of high-performance green concrete.

2. Material and methods

2.1. Material

2.1.1. Chemical composition and particle size

The materials used in this study include ASTM Type I white portland cement (wPC), limestone powder (LS), freshwater diatomite (DE), and gypsum (Gyp). Table 1 lists their chemical compositions, specific surface areas (SSA), and particle sizes (D_{50} and D_{90}). The SSA of the raw materials was measured using N_2 sorption isotherms. Rietveld refinement shows that the wPC (Lehigh, United States) contains 57.3% C_3S,[1] 30.1% C_2S, 4.6% C_3A, 1.6% $C_4A_3\$$ (ye'elimite), 3.1% calcium sulfates, and 0.2% free lime (C_4AF is below the detection limit). The selection of wPC is because of its low iron content compared to ordinary portland cement. Freshwater diatomite (DE, DiatomaceousEarth, United States) was used as received and its chemical composition conforms with the requirements of pozzolanic materials based on ASTM C618 (ASTM 2019). Limestone and gypsum powder (Fisher Scientific, United States), both with the certified purity of $\geq$ 99%, were used. #30–100 grade standard silica sand (0.15–0.6 mm sieve size) with a specific gravity of 2.65 was added to prepare mortar samples. Pea gravel (9.5 mm maximum size) was used as coarse aggregate and Vulcan sand (fineness modulus of 2.9) was used as fine aggregate to prepare concrete samples. A polycarboxylate ether (PCE)–based superplasticizer with 34% solid content (BASF, Germany) was used to obtain optimal workability.

2.1.2. Mix design

Tables 2 and 3 list the mix designs for paste/mortar and concrete samples, respectively. Paste/mortar samples are used for the studies of drying shrinkage and leaching to avoid the complex influences of coarse aggregates. Concrete samples are used for Cl^- permeability measurement per the ASTM standard. The compressive strength of each mix design has been reported previously (Li et al., 2019) and the average values are listed in Table 2. The workability of DE-containing paste, mortar, and concrete samples was adjusted using PCE superplasticizer, arranging from 1 to 3 wt.% of DE content. Materials with high surface area (e.g., SCMs and nano materials) noticeably accelerate the reaction of the cementitious materials and phases (Jin et al., 2021, 2019) and affect their mechanical properties at the early and/or late ages (Rossen et al., 2015). Therefore, additional cement replacement (2.5–3 wt.%) with gypsum was also considered to compensate for the influence of high-surface DE on the hydration and mechanical properties of the

Table 1
Chemical composition (wt.%), specific surface area, and particle size of white portland cement (wPC), diatomite (DE), limestone (LS), and gypsum (Gyp).

	wPC	DE	LS	Gyp
SiO_2	20.55	85.63	1.09	
Al_2O_3	4.42	3.96	0.22	
Fe_2O_3	0.26	1.04	0.15	
CaO	66.28	0.57	55.09	
MgO	0.86	0.46	0.50	
SO_3	4.10	<0.01	<0.01	
Na_2O	0.04	<0.01	0.02	
K_2O	0.20	0.14	0.01	
TiO_2	0.07	0.26	0.02	
P_2O_5	0.04	0.09	0.04	
MnO	0.01	0.02	0.01	
LOI	1.64	7.74	42.83	
Specific surface area [m^2/kg]	1183	27,800	2805	1022
D_{50} [μm]	10.94	6.77	2.98	11.03
D_{90} [μm]	36.85	28.41	8.16	23.75

[1] Abbreviation used for composition of cement: C=CaO; S=SiO_2; A=Al_2O_3; F= Fe_2O_3; \$=SO_3; and H=H_2O.

Table 2
wPC-DE-LS formulations of cement-based samples (wt.%).

	PC	DE	LS	Gyp	Drying Shrinkage	Cl Permeability	Leaching	Average 28d compressive strength of mortar (MPa;Li et al., 2019)
PC	100	–	–	–	X	X	X	50.2
5LS	95	–	5	–	X	X	X	49.9
10LS	90	–	10	–	X			46.5
10DE	90	10	–	–	X	X	X	52.5
20DE	80	20	–	–	X	X	X	69.3
30DE	70	30	–	–	X	X	X	63.0
20DE-5LS	75	20	5	–	X			69.9
30DE-5LS	65	30	5	–	X	X	X	71.4
20DE-5LS-3CH_2$	72	20	5	3	X			68.4
30DE-5LS-3CH_2$	62	30	5	3	X			72.1

Table 3
Mix proportions of concrete samples

w/b = 0.49	Mix proportions (kg/m^3 of concrete)							28d compressive strength (MPa) (Li et al., 2019)
	wPC	DE	LS	Aggregates		PCE	Water	
				Fine	Coarse			
wPC	433	–	–	901	784	2.5	210	35.5
5LS	410	–	22	208	181	2.5	210	36.5
10DE	386	43	–	208	181	3.9	210	40.9
20DE	339	87	–	208	181	4.8	210	46.7
30DE	294	130	–	208	181	6.1	210	48.9
30DE-5LS	272	130	22	208	181	6.0	210	50.2

composite. The nomenclatures for different mix designs are labeled 'xDE-yLS-zGyp, representing 'x' wt.% DE, 'y' wt.% LS, and 'z' wt.% Gyp replacement for cement. Replacement with LS was also considered to mimic pre-blended limestone cement that is popular in industrial applications. The durability tests in accordance with the paste and mortar formulations are also included in Table 2.

2.2. Material characterization

2.2.1. X-ray diffraction

XRD was performed on the raw DE to identify its mineralogy. Approximately 0.2 g of DE powders were packed into a sample holder, and the measurements were taken on a PANalytical Empyrean X-ray diffractometer (Malvern Panalytical Ltd., Malvern, United Kingdom) with Co-Kα radiation (λ = 1.79 Å) at 40 kV and 40 mA. Scans were performed at 5–80° 2θ using a PIXcel3D detector.

2.2.2. Infrared spectroscopy (FTIR)

The infrared spectroscopic experiment was conducted using a spectrometer (Thermofisher, United States). The raw DE powder was directly measured in the attenuated total reflectance mode in the wavelength range of 400–4000 cm^{-1}, and 20 spectra were taken and averaged.

2.2.3. Helium ion microscopy (HIM)

A Zeiss ORION NanoFab microscope was used to image the DE powder sample. The HIM accelerating voltage was 30 kV, and the beam current was ~0.6 pA. DE powder was not coated; thus, an electron flood was applied on the sample to compensate charging. The voltage of flood gun was 1300 eV with a flood time of 1000 μs.

2.2.4. Scanning electron microscopy

For back-scattered electron (BSE) imaging, all samples were soaked with isopropanol (>99% purity) to stop the hydration. Subsequently, the samples were sawed and embedded in EPO-TEK 301 epoxy (Epoxy Technology, United States) at room temperature. The embedded samples were polished down to 25 nm fineness using SiC paper and polishing cloth with kerosene (>99% purity) as the lubricant. The samples were then vacuum-coated with a 25-nm-layer of carbon. BSE images were taken with a Zeiss MA10 scanning electron microscopy (SEM), operated at 15 kV and 1 nA and equipped with an EDAX detector for chemical composition analysis. Energy dispersive X-ray spectroscopy (EDS) analysis was taken with an acquisition time of 20 s per point. For secondary electron imaging, dried samples were carefully fractured and sputtered with a 20-nm-layer of gold. Secondary electron images were taken using an FEI Quanta 200 SEM.

2.2.5. Thermogravimetry analysis

Thermogravimetric analysis (TGA) data were collected using a Hitachi STA 7300 thermal analysis system. For each sample, ~25 mg of fine powder was loaded in an alumina crucible. Each sample was heated from 40 to 1000 °C at a rate of 20 °C/min under a flow of N_2 at a velocity of 50 mL/min.

2.2.6. Mercury intrusion porosimetry

Mercury intrusion porosimetry (MIP) was used to measure the sample's porosity. Before the measurement, cylindrical hydrated pastes (w/b = 0.5) were cured for 3 day, and carefully sawed, treated with isopropanol (>99% purity) to stop hydration, and dried in a N_2-filled oven at 40 °C. The porosity measurements were performed using an AutoPore IV 9500 porosimeter with a maximum pressure of 200 MPa (Micromeritics, United States).

2.3. Durability test

2.3.1. Leaching

Accelerated leaching test of pastes samples was conducted using ammonium nitrate solution, modified from (Kamali et al., 2008). Φ25 × 25-mm paste cylinders with water-to-binder (w/b) of 0.5 were prepared and sealed in 1-L plastic containers at 100% relative humidity (RH) and 25 °C. After 24 h, the cylindrical pastes were demolded and cured at 100% RH and 25 °C until 28 days. The cylinders were then stored in sealed plastic containers with 6 M ammonium nitrate solution (Fisher Scientific, Waltham, MA, USA) at a liquid-to-solid mass ratio of 6.5. The cylinders were placed on Teflon grids to ensure a homogeneous decalcification of the specimens. The specimens were under leaching at 25 °C for 7, 14, 21, 28, and 56 days. Subsequently, the specimens were sawed, lubricated with kerosene of >99% purity (Fisher Scientific, Waltham, MA, USA), and sprayed with phenolphthalein (95 vv.%, Fisher Scientific, Waltham, MA, USA) solution to determine the depth of leaching.

2.3.2. Rapid chloride permeability

Rapid chloride permeability experiment was performed per ASTM C1202–17 using the PROOVE'it test system (Germann Instruments, Denmark) at 24 ± 1 °C. Concrete cylinders (100 mm × 200 mm) with a w/b ratio of 0.49 were cured at 100% RH and 22 ± 1 °C for 28 and 90 days. Concrete slices of 50-mm-thickness and 100-mm-diameter were sawed and lubricated with kerosene of >99% purity (Fisher Scientific, Waltham, MA, USA). Two slices were prepared for each mix, and 60 V direct current (DC) was applied on the slice. Temperature was monitored continuously to prevent overheating the sample. The total charge passed, in coulombs, of each slice was recorded for every 6 h.

2.3.3. Drying shrinkage

The drying shrinkage test was performed in accordance with ASTM C596 at 50% RH and 24 ± 1 °C. Mortar bars with the size of 25 × 25 × 285 mm were cast at a w/b ratio of 0.5 and kept a constant sand-to-binder ratio of 2.0. The mortar bars were demolded after 24 h and cured in saturated lime water for another 48 h at 24 ± 1 °C. Shrinkage of four specimens for each mix design was continuously measured from 7 days up to 365 days as recommended in ASTM C596 using a length comparator (Humboldt, United States).

3. Results and discussion

3.1. Material characterization

3.1.1. Characterization of DE

The X-ray diffractogram and FTIR spectrum of raw DE are shown in Fig. 1(a) and (b). The only crystalline impurity of the raw DE is montmorillonite (Mt with a chemical formulation of $(Na,Ca)_{0.3}(Al,Mg)_2Si_4O_{10}(OH)_2 \bullet nH_2O$). The amorphous content of DE shows structural similarity to opal (hydrated amorphous silica). The bands at 3622 and 3395 cm^{-1} in the FTIR spectrum are attributed to the vibration of —OH groups of diatomite biosilica (Sprynskyy et al., 2010). The band at 1620 cm^{-1} is attributed to H—O—H of diatomite and montmorillonite (Liu et al., 2013). The bands at 1040 and 795 cm^{-1} are assigned to the asymmetric and symmetric stretching of Si—O—Si of diatomite, respectively (Khraisheh et al., 2005). The band at 915 cm^{-1} is assigned to the Si—O of diatomite and Al—OH of montmorillonite. The bands at 518 and 441 cm^{-1} are attributed to Si—O—Al(IV) vibration and Si—O—Mg of montmorillonite (Liu et al., 2013). The band at 691 cm^{-1} could be due to the vibration of Mg—OH of montmorillonite (Neumann et al., 2011).

The images of raw DE without coating taken by helium ion microscopy are shown in Fig. 1(c) and (d). Most species in the raw DE biosilica have tubular microstructure with orderly arranged nanopores on the tube walls. The pores are mostly empty with a small amount of DE debris. The surface of the tubular biosilica is relatively smooth. To our knowledge, this study, for the first time, imaged the surface of tubular biosilica without coating using helium ion microscopy. SEM imaging of DE biosilica in exiting literature could not achieve such a very high resolution, and the coating materials used for SEM may alter/cover the fine morphological features of samples (Scrivener et al., 2016).

3.1.2. 3.1.2 Microstructure and hydration product of samples at 28 days of hydration

Fig. 2 compares the microstructure of pastes at 28 days of hydration. For plain white cement paste (wPC), portlandite (CH) crowds and many CH micro-platelets were observed in the matrix, whereas only a few micro-platelets were observed in the sample with 30% DE substitution

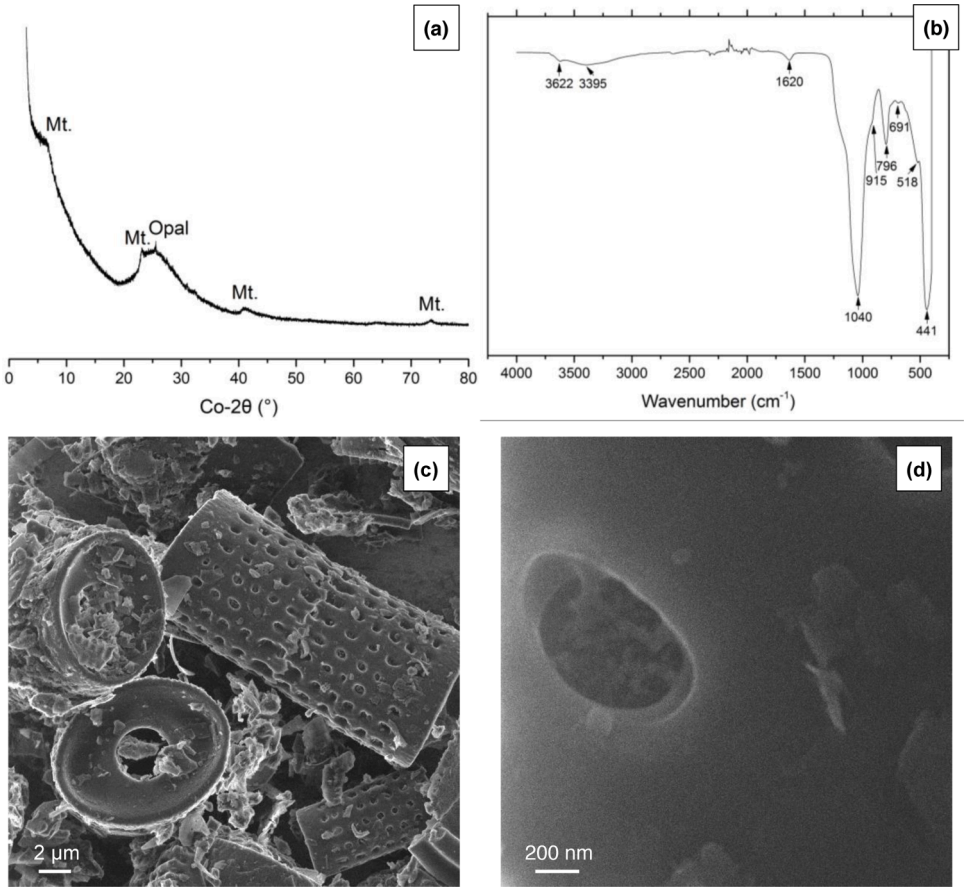

Fig. 1. Characterization of raw DE: (a) XRD result, Mt. = montmorillonite; (b) FTIR spectrum; (c) helium ion microscopy images of as-received raw DE; and (d) enlargement of pore region on the wall of a DE tube. The surface of DE is relatively smooth. No coating material was applied on the sample.

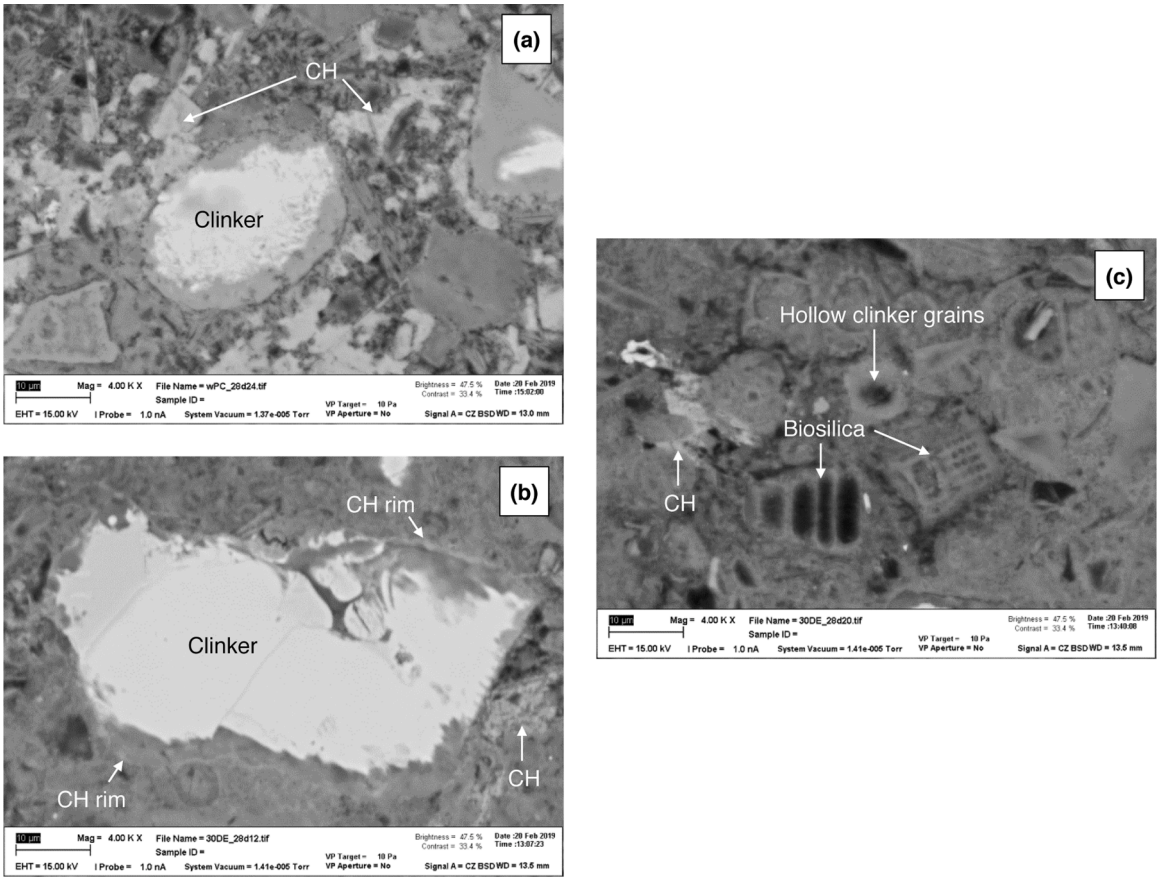

Fig. 2. Microstructure of blends after 28 days of curing: (a) wPC; (b) and (c) 30DE.

(30DE). The lower amount of cement hydration product CH in 30DE is due to lower cement content and the pozzolanic reaction between DE amorphous biosilica and lime-rich pore solution. A rim of CH precipitated between the C—S—H shell and the clinker grain in 30DE. Similar morphology was found in cement paste with high replacement levels of silica fume (Rossen et al., 2015). It is explained that the precipitation and growth of CH were favored by the spatial availability or the lower silicate concentration around clinker grains. The replacement of cement with DE results in more fully hydrated hollow small clinker grains ("Hadley grains"), which could be because biosilica provides more nucleation sites for C—S—H, leading to the formation of more outer product (OP) and less inner product (IP;Rossen et al., 2015). This fact suggests that DE promotes the silicates hydration. The 30DE system also had finer capillary pores due to C—S—H formation from more nucleation sites, whereas many coarse capillary pores were observed in wPC at 28 days. Most biosilica tubes were bonded with OP C—S—H in the matrix, indicating that the interface between OP and biosilica walls does not behave as a weak area in the DE-containing matrix. Note that the empty cores in a few DE grains have not been fully filled with hydration products.

Table 4 presents the Ca/Si molar ratios at OP and IP regions of wPC and 30DE at 28 days of hydration. The Ca/Si ratios of both IP and OP in wPC are mainly ~2.0, consistent with previous SEM-EDS studies of pure PC systems (Famy et al., 2002a,b). The comparable Ca/Si between OP and IP in wPC can be explained by the well-distributed lime-rich pore solution in the system (Taylor, 1990). The Ca/Si ratios of both IP and OP in 30DE are below 2.0, confirming a high degree of pozzolanic reaction between biosilica and lime. Ca/Si of OP is significantly lower than that of IP since the Si concentration in the pore solution of DE-rich paste is significantly higher than that in plain cement paste (Lothenbach et al., 2014), hence the Ca concentration in pore solution is reduced by biosilica. The Ca/Si of regions near biosilica (in ~500 nm) is mainly <1.0, which is lower than the OP of 30DE. Pozzolanic reaction also occurs within the biosilica grains, possibly because the porous biosilica behaves as reservoirs for lime-rich pore solution at the beginning of hydration and ion diffusion of lime and silicate in the pore solution is also expected to continue at later ages of hydration.

Table 4
Ca/Si molar ratios of hydration products in selected regions at 28 days.

		Ca/Si	Standard deviation
wPC 28d	IP	1.91	0.1
	OP	2.09	0.18
30DE 28d	IP	1.68	0.13
	OP	1.38	0.22
	DE	0.64	0.38

Fig. 3 shows the TGA results of samples at 28 days of hydration. Table 5 lists the amount of CH, amorphous $CaCO_3$, and calcite, based on the TGA results (Scrivener et al., 2016). The band at ~100 °C represents the dehydration of C—S—H and ettringite. The shoulder at ~200 °C corresponds to the dehydration of AFt (ettringite) and AFm phases (e.g., monosulfate and monocarbonate;Gruskovnjak et al., 2008). The negligible amount of AFt/AFm in 30DE-5LS is due to the low C_3A content caused by the low cement content. The band at ~460 °C represents the decomposition of CH (L'Hopital et al., 2016). The amount of portlandite decreases with an increase of DE in the blends due to the pozzolanic reaction and lower cement content. The degree of carbonation, represented by amorphous $CaCO_3$ at ~650 °C (Liu et al., 2019), is negligible in the blends. The TGA results show similar phase compositions between 30DE-5LS and 30DE, suggesting that additional 5% LS has a limited effect on the phase composition of the samples after 28 days of hydration.

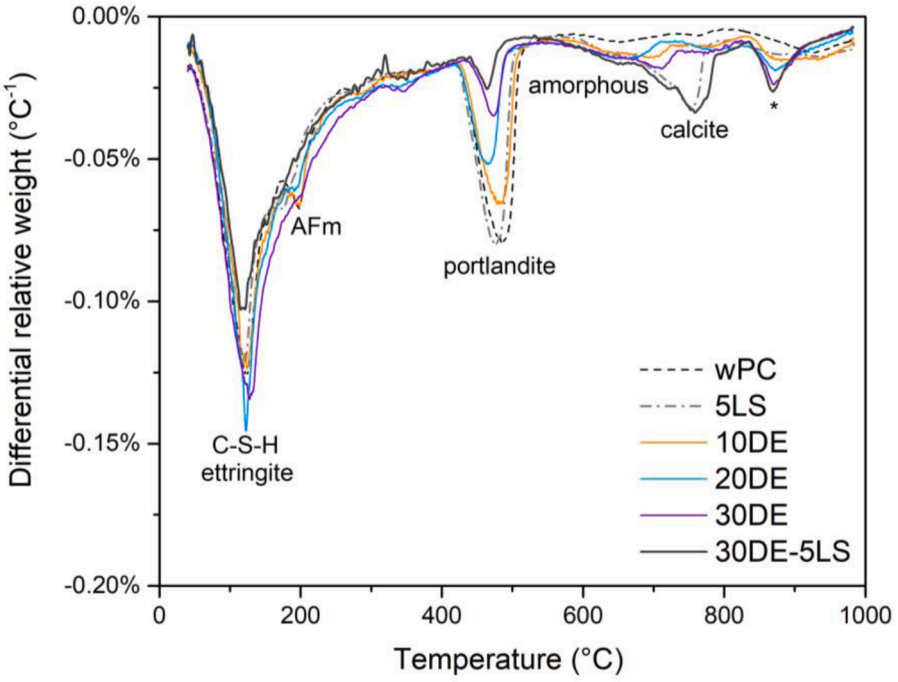

Fig. 3. TGA of hydrated pastes at 28 days of hydration. The '*' represents the decomposition of C—S—H into wollastonite ($CaSiO_3$).

Table 5
Mass fraction of portlandite, amorphous $CaCO_3$, and calcite.

	With respect to PC (wt.%)			With respect to paste (wt.%)		
	Portlandite	Amorphous $CaCO_3$	Calcite	Portlandite	Amorphous $CaCO_3$	Calcite
wPC	17.67	0.46	–	11.78	0.31	–
5LS	16.33	0.45	2.03	10.34	0.28	1.28
10DE	14.32	0.91	–	8.59	0.55	–
20DE	9.37	0.92	–	5.00	0.49	–
30DE	4.70	1.94	–	2.19	0.91	–
30DE-5LS	2.48	1.44	3.88	1.08	0.62	1.68

3.2. Durability study

3.2.1. Leaching

After 28 days of curing, the paste samples were soaked into 6 M NH_4NO_3 solution for another 28 days for the leaching test since the leaching rate in NH_4NO_3 solution is ~300 times faster than in deionized water (Heukamp et al., 2001). Fig. 4 shows the leached depths of pastes, and the pastes exhibited different rates of color change after phenolphthalein spraying. Except for 30DE-5LS, the color evolution of all pastes occurred within 3 s after spraying, whereas the color change for the 30DE-5LS developed much slower. Illustrated in Fig. 4, the leached fronts indicated by phenolphthalein for wPC and 5LS pastes were blurry, while the leached fronts for other pastes were much clearer. This difference indicates more homogeneous leaching kinetics and homogenous base environment of DE-containing pastes relative to the control groups without DE inclusion. The light-pink rims of wPC and 5LS indicate residual portlandite and clinker in the leached region.

Fig. 5 describes the evolution of leached depth, determined by phenolphthalein at different leaching ages. Initial leaching was not observed for any paste prior to the leaching test. At 7 days of leaching, all DE-containing samples exhibited lower leached depth than the samples with DE (control groups, wPC and 5LS). This result indicates that the micro and nano voids/pores of raw DE do not reduce the resistance to NH_4NO_3-induced decalcification. Despite the pH of DE-containing samples reduced by pozzolanic reaction between lime and biosilica, the refined microstructure induced by pozzolanic reaction in the sound interior regions (red in Fig. 4) enhances the resistance to NH_4NO_3-induced decalcification. After more than 14 days of leaching, 20DE and 30DE exhibited the highest resistance to leaching, suggesting a further refined microstructure by pozzolanic reaction in the sound interior region of the DE-containing pastes. The microstructure refinement overwhelms the lower cement content and/or decreased pH and results in enhanced resistance to long-term NH_4NO_3-induced decalcification.

Limestone powder has a time-dependent effect on the resistance to leaching. At 7 days, 5LS exhibited lower leached depth than wPC. Due to the reduced cement content in 5LS, the negative effect of the inclusion of 5 wt.% LS in 5LS samples is manifested after leaching for more than 14 days. Since both wPC and 5LS samples were fully leached at 56 days, their leaching resistance at 56 days is incomparable. The comparison between 30DE and 30DE-5LS at all leaching ages suggests a similar phenomenon that an additional 5% LS in 30DE-5LS causes a higher leached depth and hence a lower resistance to leaching.

BSE analyses were performed on the wPC and 30DE samples that were leached for 28 days. The result, as shown in Fig. 6, illustrates the relationship between the leaching resistance of these two samples and their microstructure. The leached exterior of wPC is extremely porous with interconnected pores of 10–20 μm. Partially reacted clinker grains were observed in the leached exterior of wPC, and a small amount of CH was also observed. This observation suggests that the resistance to leaching was mainly controlled by the paste microstructure (Burlion et al., 2006), rather than the calcium content or the basicity in the matrix. The dark regions in Fig. 6a are heavily leached grains, as evidenced by an average Ca/Si ratio of ~0.34 (see Fig. 7, at ~0 mm, sample

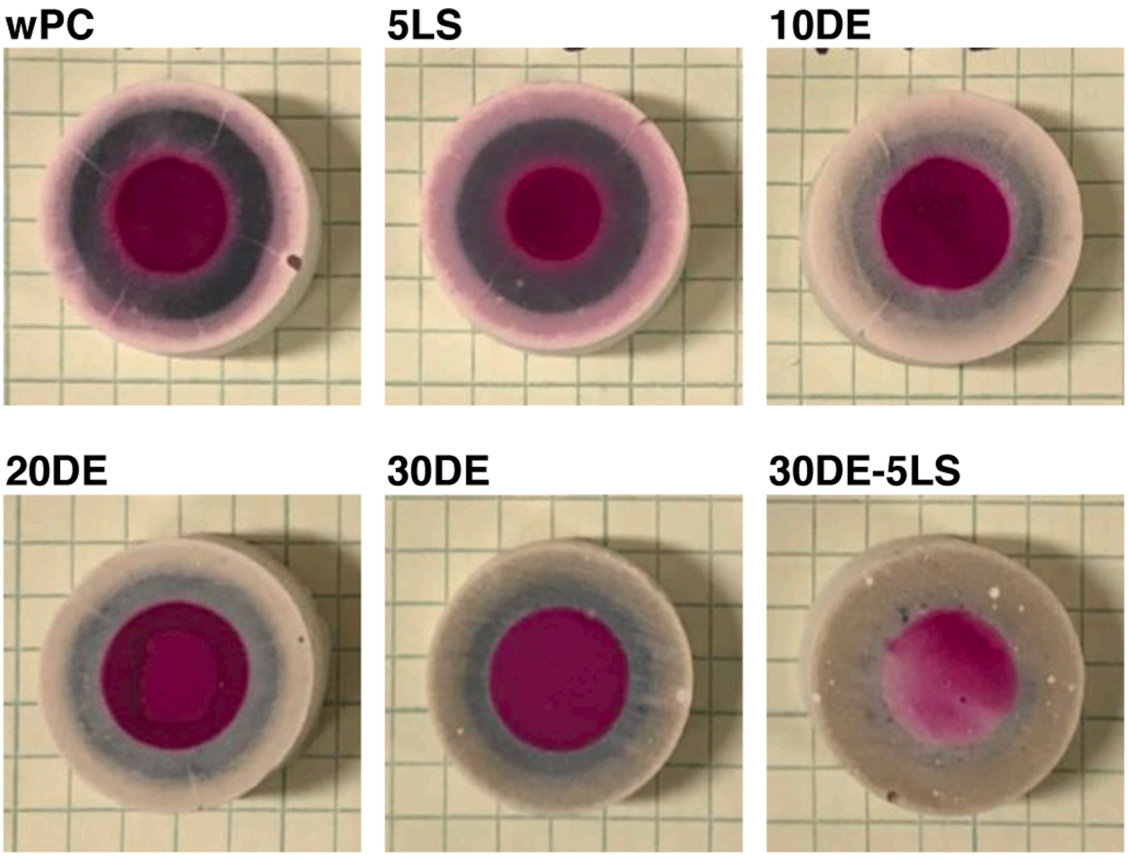

Fig. 4. Sample appearance after phenolphthalein spraying. The pastes were cured for 28 days then leached for additional 28 days. The side length of the grids is 5 mm.

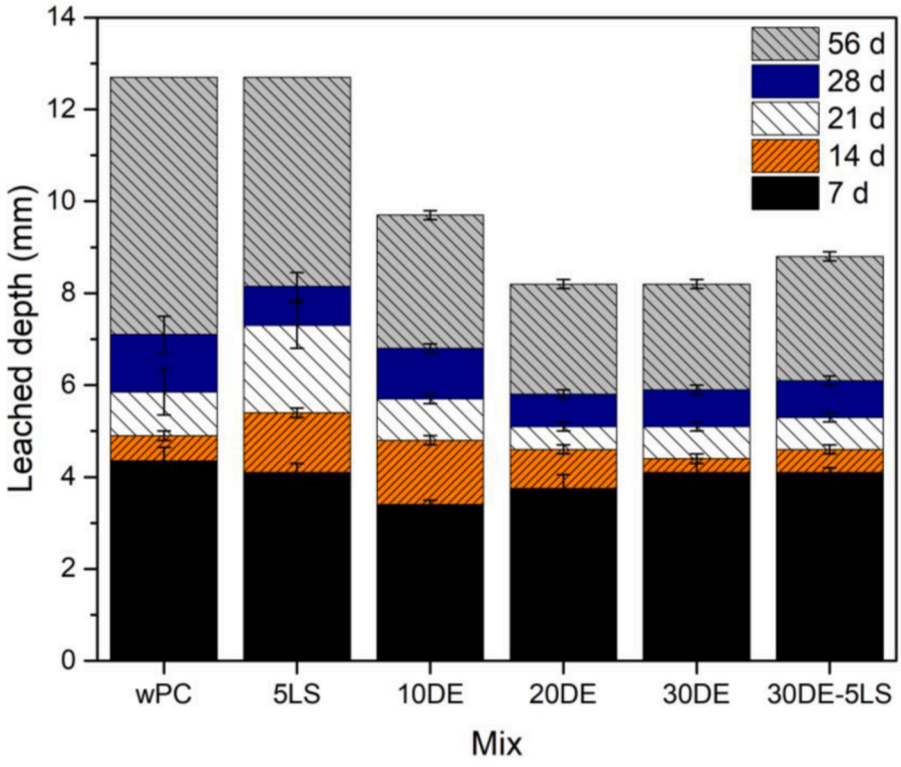

Fig. 5. Leached depth of 28d hydrated pastes for 7–56 days of leaching.

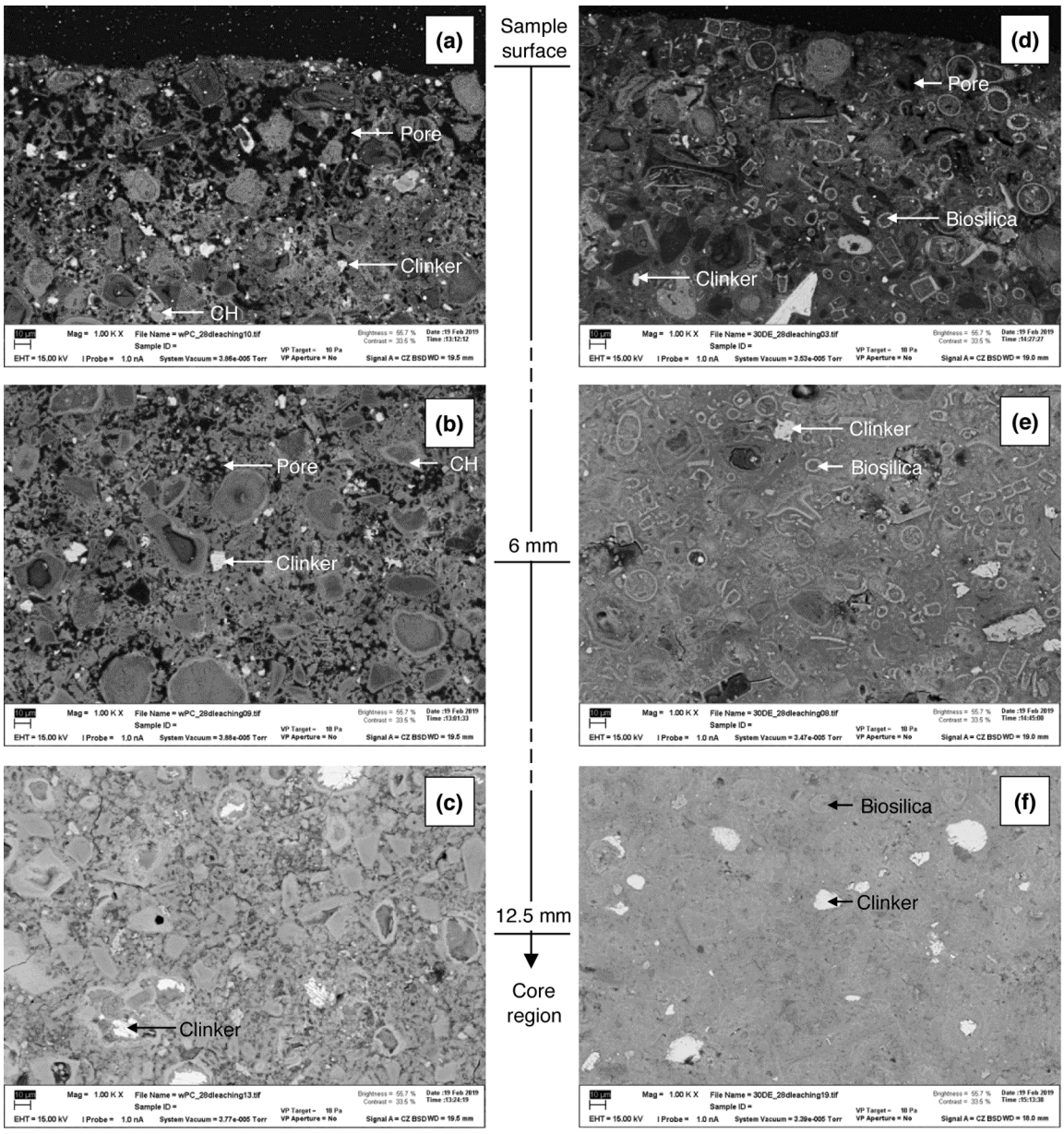

Fig. 6. BSE images of 28-day pastes leached by 6 M NH_4NO_3 for 28 days. (a) Leached exterior of wPC; (b) intermediate leached region of wPC; (c) core region of wPC; (d) leached exterior of 30DE; (e) intermediate leached region of 30DE; (f) core region of 30DE. The working distance, brightness, and contrast were fixed when taking the BSE images for either paste and thus the brightness of the images reflects the density (average atomic number) of the paste. (a) and (d) look much darker than (c) and (f) because the top row was taken in the areas nearer to the exposure surface and the pastes leached to a higher level.

surface). This value is significantly lower than the typical Ca/Si ratio of C—S—H in a mature plain paste, which is ~2.0 (Monteiro et al., 2019). Such a low Ca/Si indicates a collapsing C—S—H nanostructure as the Ca/Si ratio of calcium silicate basal layers of C—S—H is 0.67 (Ortaboy et al., 2017). The intermediate leached region in Fig. 6b is brighter with finer interconnected pores (up to 10 μm) than the exterior leached region. The high brightness suggests a low degree of Ca leaching in this region, as evidenced by the EDS result that the Ca/Si ratio of partially leached C—S—H is ~0.77. Although the core region of wPC turned pink/reddish after spraying phenolphthalein, the region has already partially degraded with microcracks and micron-size pores, as shown in Fig. 6c. The Ca/Si ratio of C—S—H in the core of leached wPC is ~1.0, lower than Ca/Si of C—S—H in wPC at 28 days in Table 4 and in PC (Richardson, 1999), suggesting the C—S—H has been considerably degraded (Jia et al., 2019).

Compared to wPC, the leached exterior of 30DE, shown in Fig. 6d, is less porous, and interconnected micropores and CH are not observed. The Ca/Si ratio of leached C—S—H in 30DE exterior is ~0.48, higher than the value, 0.34, of leached wPC exterior. The microstructures of intermediate (colored interface in Fig. 4) and core regions of leached 30DE are much denser than those of wPC. Microcracks and interconnected pores were not observed in the core of 30DE after 28-day leaching. The Ca/Si ratios of leached C—S—H in intermediate and core regions of 30DE are ~1.1 and 1.5, respectively. Both values are higher than those of C—S—H in wPC after 28-day leaching. The higher Ca/Si of leached C—S—H in 30DE can be explained by the denser microstructure prior to leaching, as evidenced in Fig. 2.

The Ca/Si ratios of both leached C—S—H and the bulk (including biosilica, leached clinker, and C—S—H) in wPC increase as the distance from the liquid/solid interface increases. The Ca/Si of leached C—S—H of wPC is lower than the bulk Ca/Si (see Fig. 7) because CH and unreacted clinker exist in bulk. The Ca/Si ratios of both leached C—S—H

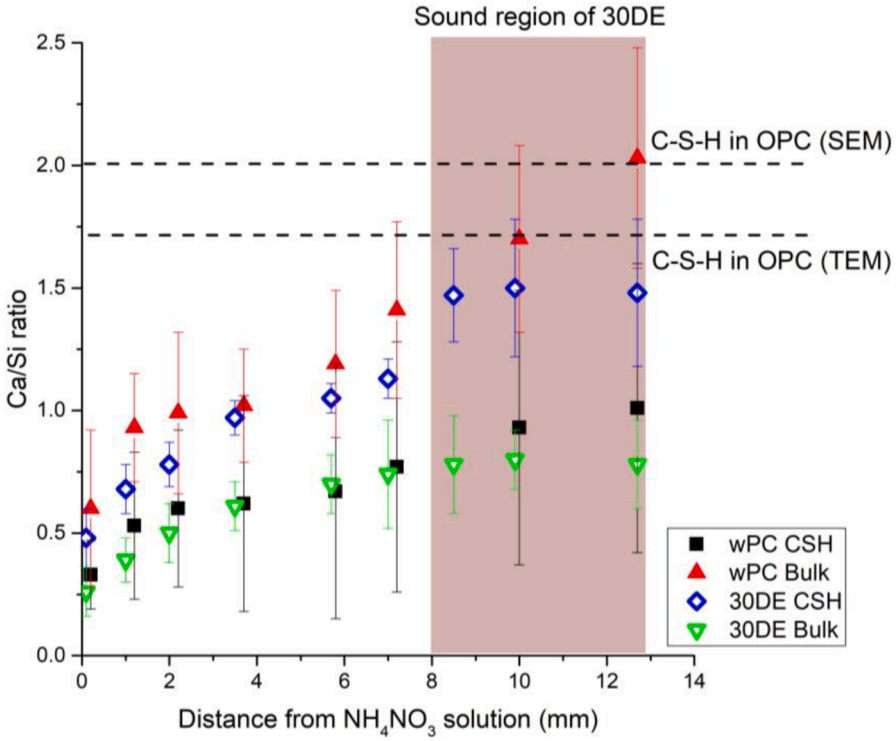

Fig. 7. Ca/Si molar ratio of matrix of 28-day pastes leached for 28 days. CSH region is a C—S—H-rich zone excluding portlandite and residual unreacted clinker grains, while the bulk region includes leached C—S—H, portlandite, and clinker grains. The Ca/Si of pure C—S—H in ordinary Portland cement (OPC) is typically 1.7–2.0 (Monteiro et al., 2019), between the dash-lines.

and the bulk in 30DE also increase with increasing distance from the liquid/solid interface but plateau at ~1.5 in the sound region (red region in Fig. 4, >10 mm to the interface). The Ca/Si of leached C—S—H in 30DE is higher than the leached bulk of 30DE because cement was replaced with silica-rich diatomite. The deviation of Ca/Si of wPC is significantly greater than that of 30DE, suggesting that the decalcification of 30DE is more homogenous than of wPC due to a refined microstructure. The microstructure homogeneity of matrix is important for the resistance to leaching (Mehta and Monteiro, 2017).

3.2.2. 3.2.2 Rapid chloride permeability

Fig. 8 shows the matrix and interfacial transition zone (ITZ) of wPC control and 30DE concrete after 28 days of curing. Bright bands of CH and dark bands of porous microstructure were both observed in the ITZ of wPC concrete (Fig. 8a and b). The ITZ of wPC is ~20–60 μm thick, which is a typical range in normal concrete without incorporation of SCMs (Mehta and Monteiro, 2017). The matrix of wPC concrete is CH-rich and relatively porous compared to 30DE concrete as shown in Fig. 9b, consistent with the microstructure of wPC paste (Fig. 6). CH was not observed in the ITZ of 30DE concrete, and the ITZ is significantly thinner and denser compared to wPC concrete. This observation could be due to the pozzolanic reaction between amorphous silica and lime, which in turn lower the lime concentration in pore solution (Duan et al., 2013). The matrix of the 30DE concrete is much denser than that of wPC concrete and exhibits less CH due to the pozzolanic reaction between biosilica and lime in the pore solution. The absence of The Ca/Si of ITZ of 30DE is mostly <2.0, which is also consistent with 30DE paste (Section 3.2.1). The DE grains in 30DE matrix are densely packed.

Fig. 9 shows the rapid Cl^- permeability, which is defined by total passed charge, for each sample at 28 and 90 days. For wPC sample that is replaced by 5 wt.% LS (5LS), the quantity of total passed charge in the 28-day hydrated 5LS concrete sample was 300 C lower than that of the plain wPC sample (control). The reduced Cl^- permeability of 5LS concrete is attributed to the refined pore structure due to the fine particle size of LS and the possible reaction between calcite and aluminates (Celik et al., 2014; De Weerdt et al., 2011). The total passed charge of 28-day hydrated 10DE concrete decreased by 64% compared to wPC control. The nano and micro pores of biosilica are unlikely to affect the resistance to Cl^- permeability. The total passed charges of 28-day hydrated 20DE and 30DE concrete were 76% and 92%, respectively, lower than that of the control group. 30DE-5LS concrete with additional replacement of cement by LS exhibited comparable Cl^- permeability to 30DE at 28 days of hydration. Based on the microstructure analysis shown in Fig. 8, one can infer that the significantly reduced Cl^- permeability with an increased level of DE blends is attributed to the refined pore structure in the matrix and ITZ (Sivasundaram et al., 1995; Wu et al., 2020), as well as to an increased amount of C—S—H from pozzolanic reaction for Cl^- binding (Tang and Nilsson, 1993).

The total passed charge of wPC at 90 days was 10% lower than at 28 days. The total passed charge of 5LS reduced by 6% from 28 to 90 days, showing a similar trend in Cl^- permeability as the control group. The slightly lowered Cl^- permeability at 90 days compared to 28 days is due to further hydration of cement, which leads to higher C—S—H content and refined pore structure. The total passed charges of 10DE, 20DE, and 30DE reduced by 32%, 54%, and 66%, respectively, from 28 to 90 days. The increased reduction in Cl^- permeability with higher levels of DE can be explained by increased amounts of C—S—H from pozzolanic reaction and increasingly refined pore structure (Chopra and Siddique, 2015; Mastali et al., 2019). Similar to 28 days, 30DE-5LS concrete with additional replacement of cement by LS exhibited comparable Cl^- permeability to 30DE at 90 days of hydration.

3.2.3. Drying shrinkage

Table 6 lists the drying shrinkage of wPC, 5LS, 10LS, and DE-containing mortars. The drying shrinkage shows a rapid development during the first 21 days of hydration. The replacement of wPC with LS decreases the drying shrinkage, and 10LS mortar exhibits less drying shrinkage compared to 5LS at all ages due to a lowered cement content

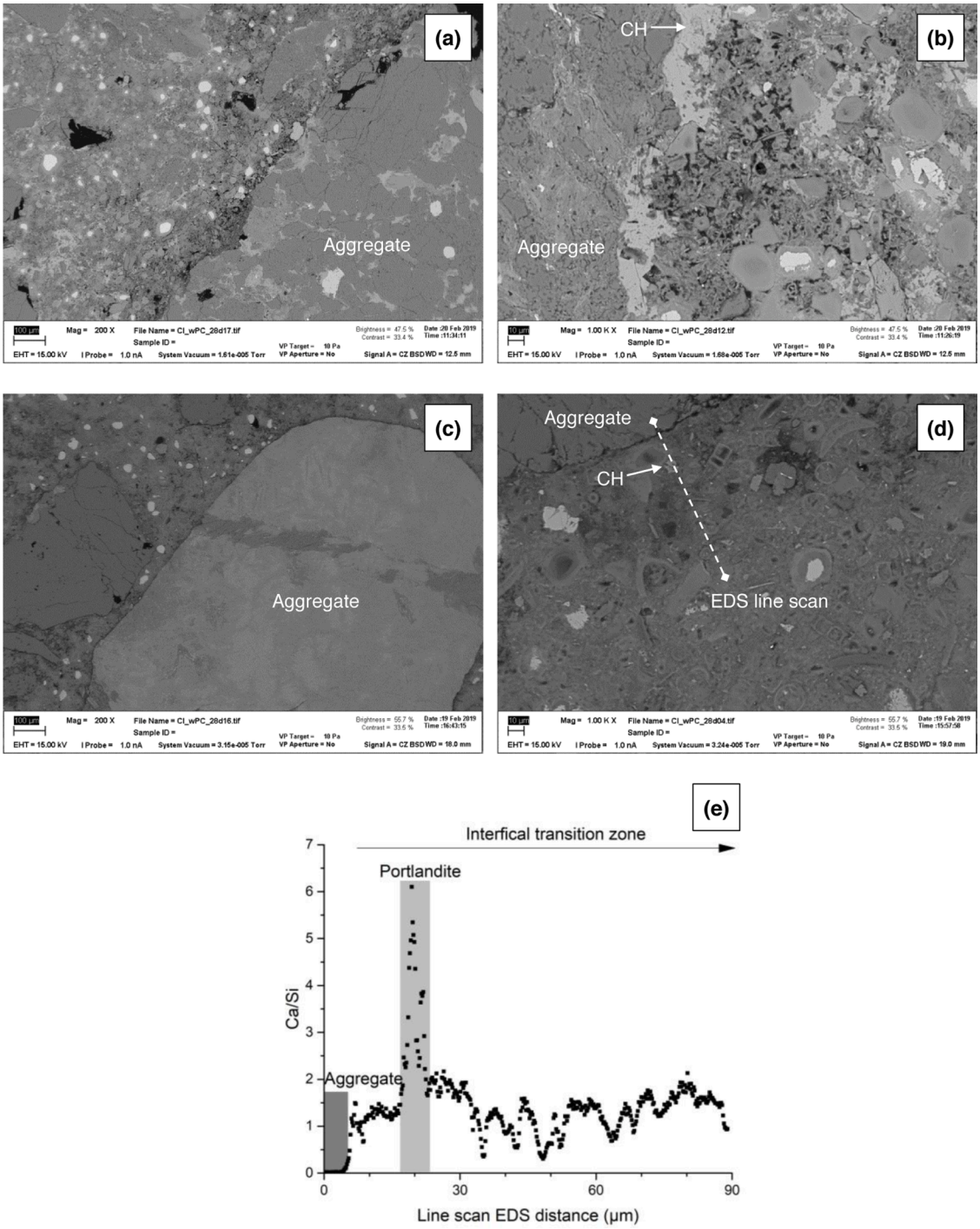

Fig. 8. BSE images of (a)-(b) ITZ of wPC concrete at 28days, (c)-(d) ITZ of 30DE concrete at 28 days, and (e) Ca/Si molar ratio of ITZ in (d).

in 10LS-containing mortars. The replacement of wPC with DE significantly increases the drying shrinkage, particularly during the first 14 days, and the drying shrinkage was more pronounced with higher DE levels at all ages. This fact is due to the refined pore structure by the pozzolanic biosilica, which has also been observed for fine pozzolans (e.g., silica fume and rice husk ash;Rao, 2001;Habeeb and Fayyadh, 2009; Yang et al., 2019;Junior et al., 2019). Compared to 20DE mortar, the additional 5 wt.% LS exhibits limited effect on the development of drying shrinkage at all ages. This similar devolvement of drying shrinkage is also observed in 30DE and 30DE-5LS. However, the additional 3 wt.% gypsum to 20DE-5LS and 30DE-5LS samples decreases the drying shrinkage.

The pore structure of samples with various levels of DE and additional LS at 3 days measured by MIP is shown in Fig. 10. The replacement of cement with 5 wt.% LS considerably lowers the total porosity compared to wPC due to the finer grains of LS (Table 7). The total porosity of 10DE is comparable to wPC and increases with an increased replacement level of DE. This phenomenon has also been observed in other cement-pozzolan replacements such as metakaolin-blended cement paste (Antoni et al., 2012) and fly ash-blended cement paste (Chindaprasirt et al., 2005). In addition to total porosity, the amount of gel pores with diameter <10 nm increases with increased DE substitution level, which is caused by an elevated degree of pozzolanic reaction that leads to a greater formation of C—S—H. All DE-blended samples

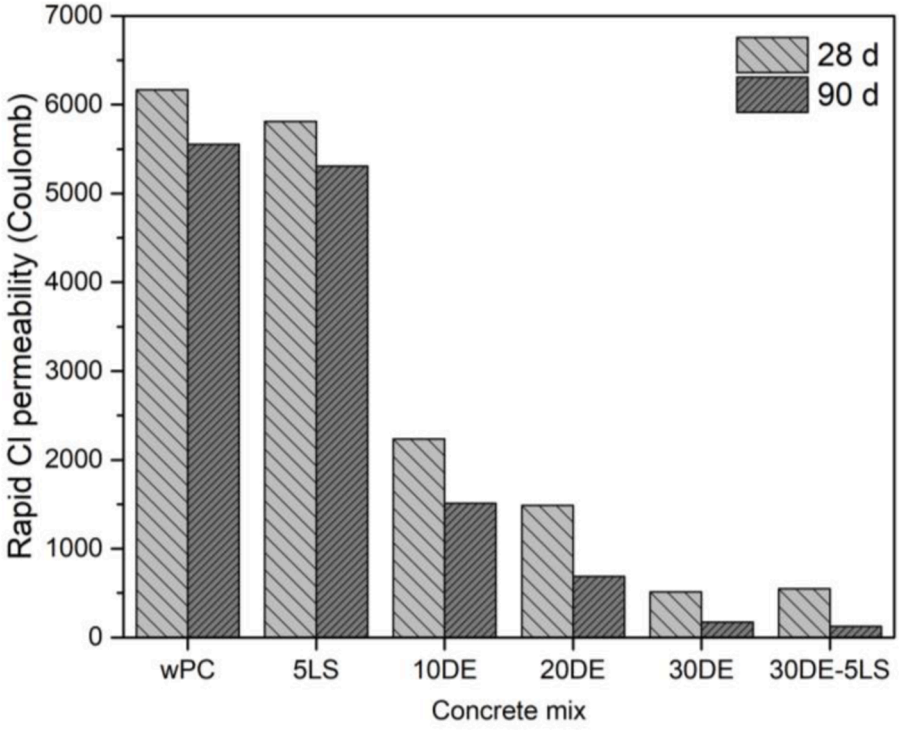

Fig. 9. Total passed charge of concrete with various mixes at 28 and 90 days.

Table 6
Strain of drying shrinkage of mortars in microstrain. The standard error varies within 50 microstrain with few exceptions not exceeding 100 microstrain.

	wPC	5LS	10LS	10DE	20DE	30DE	20DE-5LS	20DE-5LS- 3CH_2$	30DE-5LS	30DE-5LS-3CH_2$
7 d	590	543	423	718	929	1181	941	799	1101	989
14 d	881	812	767	1043	1273	1540	1281	1110	1493	1327
21 d	1150	1034	903	1219	1444	1701	1401	1221	1652	1472
28 d	1253	1133	1007	1323	1493	1778	1445	1263	1722	1540
90 d	1544	1372	1273	1619	1780	2120	1842	1667	2151	2038
180 d	1762	1544	1362	1720	1878	2219	1922	1770	2267	2183
365 d	1849	1658	1400	1793	1932	2251	1967	1811	2290	2202

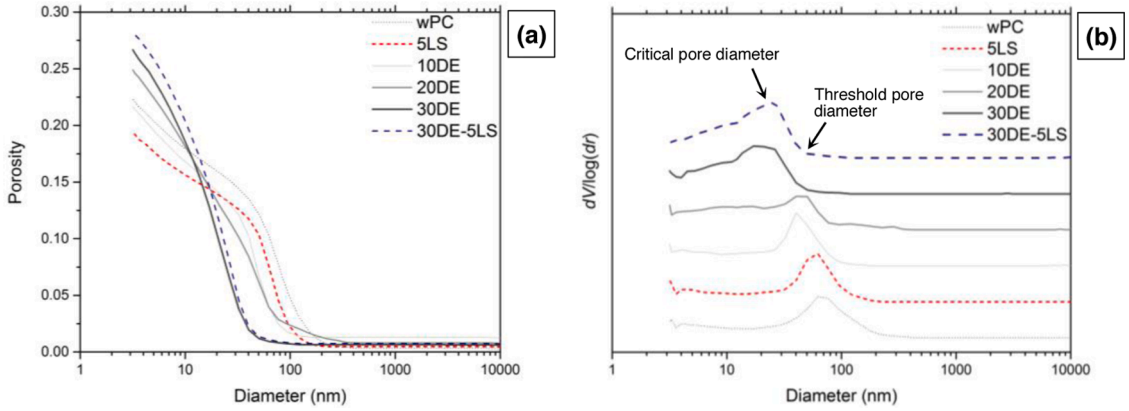

Fig. 10. Comparison of pore structure of samples at 3 days: (a) cumulative pore volume; (b) pore size distribution.

Table 7
Pore content at 3 days measured by MIP in vol%.

Pore range	wPC	5LS	10DE	20DE	30DE	30DE-5LS
Total porosity	22.3	19.5	21.7	24.9	26.7	28.3
D >10 nm	18.0	15.6	16.8	18.2	18.6	20.4
3 nm < d < 10 nm	4.4	3.9	4.9	6.8	8.1	7.9

exhibit a smaller threshold diameter than wPC control, and 30DE and 30DE-5LS exhibit a much smaller threshold radius than the other samples, suggesting much finer pore size ranges of 30DE and 30DE-5LS. The critical pore diameter decreases as DE substitution level increases, also indicating a refined pore structure by DE substitution. Again, the refined pore structure by DE substitution provides an explanation of the higher drying shrinkage of DE-containing samples compared to other

non-DE-containing samples.

The refined microstructure by partial replacement of cement with DE at 3 days of hydration is also evidenced by SEM analysis, as shown in Fig. 11. For hydrated wPC paste, the SEM images show that its microstructure is heterogeneous and porous with typical morphological features of fibrillar C—S—H (hundreds of nm long), portlandite platelets (approximately a few to tens of microns wide), and ettringite needles. For hydrated 30DE pastes, a great number of DE tubes are observed in its dense matrix. These tubes seem to be tightly bonded with the matrix (Fig. 11d). Because of the low density of raw DE and reduced cement

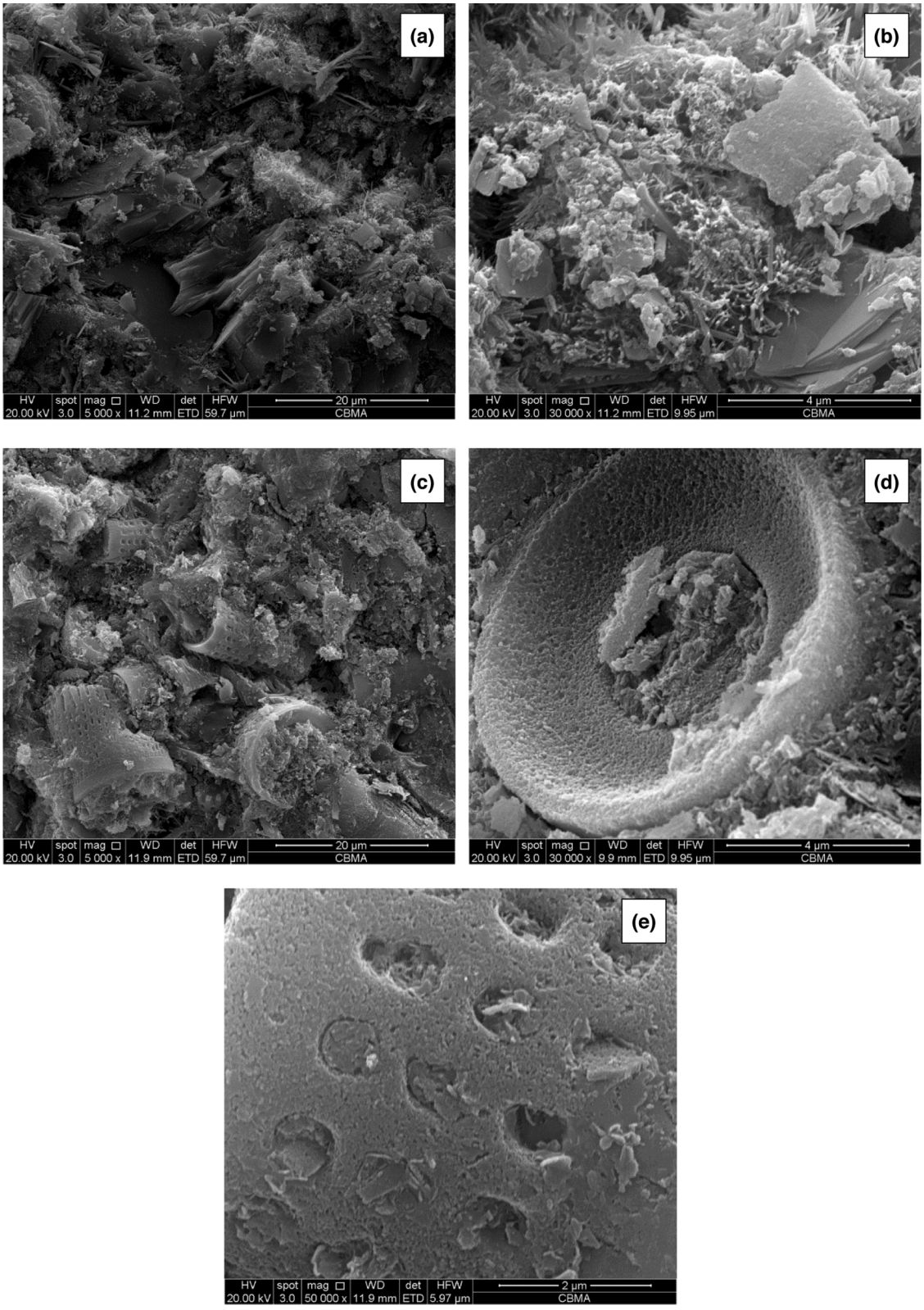

Fig. 11. Secondary electron images of fractured pastes at 3 days: (a) wPC; (b) Enlargement of wPC; (c) 30DE; (d) and (e) Enlargement of biosilica tubes in 30DE. The bulk Ca/Si molar ratio obtained in EDS analysis is 0.39.

content, 30DE with 30 wt.% DE substitution means a lowered volumetric fraction of cement compared to wPC paste (the dilution effect (Rahhal and Talero, 2005)). Therefore, fewer clinker grains, ettringite needles, and portlandite micro-platelets are observed in Fig. 11c. An enlargement of DE tubes in Fig. 11d and e shows that C—S—H homogeneously grows on the surface of DE tubes, confirming the seeding effect of biosilica during the early hydration of cement. The C—S—H on biosilica surface is not fibrillar and appears to be foil-like, suggesting a low lime concentration in the pore solution or low Ca/Si of C—S—H (Rodriguez et al., 2015). The hollow cores of biosilica tubes and pores on the tube walls are already filled with C—S—H at 3 days, indicating that the voids in biosilica could be filled during hydration. Therefore, one can infer that the initial pores that appeared in DE are unlikely to fully serve as channels for transporting fluid and/or ion (e.g., Cl^-) in the hardened DE-containing pastes. In addition, the EDS result shows the bulk Ca/Si molar ratio in Fig. 11e is 0.39, indicating the precipitation of C—S—H on the surface of DE tube. The refined microstructure evidenced by SEM is consistent with MIP analysis, both of which relate to the high drying shrinkage of DE-containing samples at early ages.

3.3. Discussion

Based on Section 3.2.1, the refined pore structure and rearranged microstructure of DE biosilica-containing samples result in the higher resistance to leaching. The lower portlandite content decreases the ion diffusivity in the leached zone and inhibits the leaching kinetics (Kamali et al., 2008). Section 3.2.2 shows that the refined pore structure induced by the introduction of biosilica decreases the Cl^- permeability of the matrix, and that the increased C—S—H also promotes the Cl^- binding and lowers the Cl^- permeability. Compared to control samples, the refined pore structure of DE-containing samples results in greater capillary tension, leading to greater drying shrinkage. Such increased drying shrinkage is more critical at early ages, leading to a higher risk of cracking for DE-containing samples. Therefore, extra care should be taken to mitigate the significant shrinkage of DE-containing cementitious materials. For example, one can use shrinkage reducing admixture and extended curing period. The high early strength of DE-containing samples could help offset the cracking potential caused by drying shrinkage (Ahmadi et al., 2018). Decision-makers should consider the advantages and limitations of using DE in designing green cement-based materials. As the DE-containing cement-based materials exhibited higher resistance to leaching, higher Cl^- impermeability, and higher drying shrinkage, they may be suitable for reinforced structures served in freshwater, seawater, or humid environments. Alternatively, DE-containing cement-based composites can serve non-reinforced structures (e.g., concrete blocks). However, decision-makers should take extra care on extended curing and the depth of concrete cover when designing reinforced DE-containing concrete. The superior properties of cement-based materials containing high-quality DE biosilica show a promising potential to use biosilica from diatom-based biofuel residues to produce high-performance bio-based concrete. For large-scale and direct demonstration in construction industry, future studies could focus on using widely available inexpensive fresh biosilica from diatom-based biofuel production.

4. Conclusion

In this study, portland cement was partially replaced by 30 wt.% diatomite (83% amorphous biosilica) and the durability performances of DE-containing cementitious composites and the underlying mechanisms were investigated and presented. The studied cementitious materials containing DE biosilica exhibit superior impermeability (e.g., ~900% improvement) and resistance to leaching at 28d. The intrinsic voids in raw biosilica are not detrimental to impermeability and chemical resistance. The use of biosilica significantly densifies the ITZ of concrete by consuming portlandite and filling porous regions (tens of microns thick) via pozzolanic reaction. The pozzolanic reaction results in greater volumes of gel pores and much finer capillary pore sizes (~80% reduction). The refined pore structure of DE-containing cementitious materials results in a superior resistance to calcium leaching and chloride permeability but higher drying shrinkage at early ages. A 5 wt.% addition of limestone powder shows no significant influence on the durability properties of the ternary binder system. This study provides valuable insight into silica-rich SCMs with porous structures, e.g., rice husk ash or other biomass products (e.g., biosilica from sugarcane bagasse ash). Microalgae-based (e.g., diatom) biofuel production is a promising source of biosilica and carbon-negative biofuel. Considering that the use of high-quality diatom-based biosilica in cement-based materials increases the strength and certain durability properties and lowers the environmental impacts of their production, biosilica-blended cement-based composites can be an enabler of the pursuit of renewable diatom-based biofuel. The successful implementation of diatom-based biofuel byproduct in concrete would help simultaneously decrease the CO_2 emissions of two carbon-intense industry sectors: energy and construction.

CRediT authorship contribution statement

Jiaqi Li: Conceptualization, Investigation, Methodology, Validation, Formal analysis, Data curation, Visualization, Project administration, Writing – original draft, Writing – review & editing. **Qingxu Jin:** Investigation, Formal analysis, Validation, Writing – original draft, Writing – review & editing. **Wenxin Zhang:** Methodology, Resources, Visualization, Writing – review & editing. **Chen Li:** Investigation, Methodology, Writing – review & editing. **Paulo J.M. Monteiro:** Conceptualization, Resources, Project administration, Writing – review & editing, Supervision, Funding acquisition.

Declaration of Competing Interest

None

Acknowledgement

This study was supported by the Republic of Singapore's National Research Foundation-Berkeley Education Alliance for Research in Singapore (BEARS) for the Singapore-Berkeley Building Efficiency and Sustainability in the Tropics (SinberBEST) program. We thank Rupert Myers at Imperial College London for his great inspiration of this research topic. Chen Li acknowledges the financial support provided by the National Natural Science Foundation of China (52102027) and Shanghai Pujiang Program (21PJ1412800). Arthur Li, Xiao Kun Lu, Jonathan Lee, and Minju Zhong at UC Berkeley are thanked for assistance in sample preparations. Yaqiang Li at Beijing University of Technology is thanked for the assistance in secondary electron imaging.

References

Abdulkareem, O.A., Ramli, M., Matthews, J.C., 2019. Production of geopolymer mortar system containing high calcium biomass wood ash as a partial substitution to fly ash: an early age evaluation. Compos. Part B 174, 106941.
Ahmadi, Z., Esmaeili, J., Kasaei, J., Hajialioghli, R., 2018. Properties of sustainable cement mortars containing high volume of raw diatomite. Sustain. Mater. Technol. 16, 47–53.
Alcaraz, J.S., Belda, I.M., Sanchis, E.J., Borrell, J.M.G., 2019. Mechanical properties of plaster reinforced with yute fabrics. Compos. Part B 178, 107390.
Antoni, M., Rossen, J., Martirena, F., Scrivener, K., 2012. Cement substitution by a combination of metakaolin and limestone. Cem. Concr. Res. 42, 1579–1589.
ASTM, 2019. ASTM C618 Standard Specification for Coal Fly Ash and Raw or Calcined Natural Pozzolan for Use in Concrete.
Brunner, E., Ehrlich, H., Schupp, P., Hedrich, R., Hunoldt, S., Kammer, M., Machill, S., Paasch, S., Bazhenov, V., Kurek, D., 2009. Chitin-based scaffolds are an integral part of the skeleton of the marine demosponge Ianthella basta. J. Struct. Biol. 168, 539–547.

Burlion, N., Bernard, D., Chen, D., microtomography, X.-., 2006. Application to microstructure analysis of a cementitious material during leaching process. Cem. Concr. Res. 36, 346–357.
Celik, K., Meral, C., Mancio, M., Mehta, P.K., Monteiro, P.J.M., 2014. A comparative study of self-consolidating concretes incorporating high-volume natural pozzolan or high-volume fly ash. Constr. Build. Mater. 67, 14–19.
Chindaprasirt, P., Jaturapitakkul, C., Sinsiri, T., 2005. Effect of fly ash fineness on compressive strength and pore size of blended cement paste. Cem. Concr. Comp. 27, 425–428.
Choi, J., Park, H., Kim, J., 2015. Strength characteristics of mortar with diatomite powder as an admixture. J. Soc. Disaster Inf. 11, 329–336.
Chopra, D., Siddique, R., 2015. Kunal, Strength, permeability and microstructure of self-compacting concrete containing rice husk ash. Biosyst. Eng. 130, 72–80.
Davis, R.E., Klein, A., 1950. The effect of the use of diatomite treated with air-entraining agents upon the properties of concrete. In: Symposium on Use of Pozzolanic Materials in Mortars and Concretes. ASTM International.
De Weerdt, K., Ben Haha, M., Saout, G.Le, Kjellsen, K.O., Justnes, H., Lothenbach, B., 2011. Hydration mechanisms of ternary Portland cements containing limestone powder and fly ash. Cem. Concr. Res. 41, 279–291.
Degirmenci, N., Yilmaz, A., 2009. Use of diatomite as partial replacement for Portland cement in cement mortars. Constr. Build. Mater. 23, 284–288.
Duan, P., Shui, Z., Chen, W., Shen, C., 2013. Effects of metakaolin, silica fume and slag on pore structure, interfacial transition zone and compressive strength of concrete. Constr. Build. Mater. 44, 1–6.
Ehrlich, H., Motylenko, M., Sundareshwar, P.V., Ereskovsky, A., Zgłobicka, I., Noga, T., Płociński, T., Tsurkan, M.V., Wyroba, E., Suski, S., 2016. Multiphase biomineralization: enigmatic invasive siliceous diatoms produce crystalline calcite. Adv. Funct. Mater. 26, 2503–2510.
Ejaz, H., Somanader, E., Dave, U., Ehrlich, H., Rahman, M.A., 2021. Didymo and its polysaccharide stalks: beneficial to the environment or not? Polysaccharides 2, 69–79.
Esen, Y., Kurt, A., 2018. Effect of high temperature in concrete for different mineral additives and rates. Ksce J. Civ. Eng. 22, 1288–1294.
Famy, C., Scrivener, K.L., Atkinson, A., Brough, A.R., 2002b. Effects of an early or a late heat treatment on the microstructure and composition of inner C-S-H products of Portland cement mortars. Cem. Concr. Res. 32, 269–278.
Famy, C., Scrivener, K.L., Crumbie, A.K., 2002a. What causes differences of C-S-H gel grey levels in backscattered electron images? Cem. Concr. Res. 32, 1465–1471.
Fragoulis, D., Stamatakis, M.G., Papageorgiou, D., Chaniotakis, E., 2005. The physical and mechanical properties of composite cements manufactured with calcareous and clayey Greek diatomite mixtures. Cem. Concr. Comp. 27, 205–209.
Gerengi, H., Kocak, Y., Jazdzewska, A., Kurtay, M., Durgun, H., 2013. Electrochemical investigations on the corrosion behaviour of reinforcing steel in diatomite- and zeolite-containing concrete exposed to sulphuric acid. Constr. Build. Mater. 49, 471–477.
Gerengil, H., Kocak, Y., Jazdzewska, A., Kurtay, M., 2017. Corrosion behavior of concrete produced with diatomite and zeolite exposed to chlorides. Comput. Concr. 19 (2), 161–169.
Graham, J.M., Graham, L.E., ZulkiXy, S.B., Pfleger, B.F., Hoover, S.W., Yoshitani, J., 2012. Freshwater diatoms as a source of lipids for biofuels. J. Ind. Microbiol. Biot. 39, 419–428.
Gruskovnjak, A., Lothenbach, B., Winnefeld, F., Figi, R., Ko, S.C., Adler, M., Mader, U., 2008. Hydration mechanisms of super sulphated slag cement. Cem. Concr. Res. 38, 983–992.
Habeeb, G.A., Fayyadh, M.M., 2009. Rice husk ash concrete: the effect of RHA average particle size on mechanical properties and drying shrinkage. Australian J. Basic Appl. Sci. 3 (3), 1616–1622.
Heukamp, F.H., Ulm, F.J., Germaine, J.T., 2001. Mechanical properties of calcium-leached cement pastes: triaxial stress states and the influence of the pore pressures. Cem. Concr. Res. 31, 767–774.
Ho, D.P., Ngo, H.H., Guo, W., 2014. A mini review on renewable sources for biofuel. Bioresour. Technol. 169, 742–749.
IEA, 2020. Global Energy Review. IEA, p. 2020.
Jia, Z., Cao, R., Chen, C., Zhang, Y., 2019. Using in-situ observation to understand the leaching behavior of Portland cement and alkali-activated slag pastes. Compos. Part B 177, 107366.
Jin, Q., Hordern, S.L., Tang, Y., Kurtis, K.E., 2021. NOx sequestration by calcium aluminate cementitious materials. Cem. Concr. Res. 142, 106381.
Jin, Q., Saad, E., Zhang, W., Tang, Y., Kurtis, K., 2019. Quantification of NOx uptake in plain and TiO2-doped cementitious materials. Cem. Concr. Res. 122, 251–256.
Junior, A.N., Ferreira, S.R., Toledo Filho, R.D., Fairbairn, E.d.M.R., Dweck, J., 2019. Effect of early age curing carbonation on the mechanical properties and durability of high initial strength Portland cement and lime-pozolan composites reinforced with long sisal fibres. Compos. Part B 163, 351–362.
Kamali, S., Moranville, M., Leclercq, S., 2008. Material and environmental parameter effects on the leaching of cement pastes: experiments and modelling. Cem. Concr. Res. 38, 575–585.
Kastis, D., Kakali, G., Tsivilis, S., Stamatakis, M.G., 2006. Properties and hydration of blended cements with calcareous diatomite. Cem. Concr. Res. 36, 1821–1826.
Khraisheh, M.A.M., Al-Ghouti, M.A., Allen, S.J., Ahmad, M.N., 2005. Effect of OH and silanol groups in the removal of dyes from aqueous solution using diatomite. Water Res. 39, 922–932.
Kim, S., Zhang, X., Reddy, A.D., Dale, B.E., Thelen, K.D., Jones, C.D., Izaurralde, R.C., Runge, T., Maravelias, C., 2020. Carbon-negative biofuel production. Environ. Sci. Technol. 54, 10797–10807.
Kurtay, M., Gerengi, H., Kocak, Y., Chidiebere, M.A., Yildiz, M., 2020. The potency of zeolite and diatomite on the corrosive destruction of reinforcing steel in 1M HNO3 environment. Constr. Build. Mater. 236, 117572.
Levitan, O., Dinamarca, J., Hochman, G., Falkowski, P.G., 2014. Diatoms: a fossil fuel of the future. Trends Biotechnol. 32, 117–124.
L'Hopital, E., Lothenbach, B., Kulik, D.A., Scrivener, K., 2016. Influence of calcium to silica ratio on aluminium uptake in calcium silicate hydrate. Cem. Concr. Res. 85, 111–121.
Li, J., Zhang, W., Li, C., Monteiro, P.J.M., 2019. Green concrete containing diatomaceous earth and limestone: workability, mechanical properties, and life-cycle assessment. J. Clean. Prod. 223, 662–679.
Li, J., Zhang, W., Li, C., Monteiro, P.J.M., 2020. Eco-friendly mortar with high-volume diatomite and fly ash: performance and life-cycle assessment with regional variability. J. Clean. Prod., 121224
Liu, D., Yuan, P., Liu, H.M., Cai, J.G., Tan, D.Y., He, H.P., Zhu, J.X., Chen, T.H., 2013. Quantitative characterization of the solid acidity of montmorillonite using combined FTIR and TPD based on the NH3 adsorption system. Appl. Clay Sci. 80-81, 407–412.
Liu, L., Sun, C., Geng, G., Feng, P., Li, J., Dahn, R., 2019. Influence of decalcification on structural and mechanical properties of synthetic calcium silicate hydrate (C-S-H). Cem. Concr. Res. 123.
Lothenbach, B., Rentsch, D., Wieland, E., 2014. Hydration of a silica fume blended low-alkali shotcrete cement. Phys. Chem. Earth 70-71, 3–16.
Luhar, S., Cheng, T.-.W., Luhar, I., 2019. Incorporation of natural waste from agricultural and aquacultural farming as supplementary materials with green concrete: a review. Compos. Part B 175, 107076.
Mastali, M., Dalvand, A., Sattarifard, A., Abdollahnejad, Z., Nematollahi, B., Sanjayan, J., Illikainen, M., 2019. A comparison of the effects of pozzolanic binders on the hardened-state properties of high-strength cementitious composites reinforced with waste tire fibers. Compos.Part B 162, 134–153.
Mehta, P.K., Monteiro, P.J., 2017. Concrete Microstructure, Properties and Materials. McGraw-Hill, New York.
Monteiro, P.J.M., Geng, G., Marchon, D., Li, J., Alapati, P., Kurtis, K.E., Qomi, M.J.A., Research, C., 2019. Advances in characterizing and understanding the microstructure of cementitious materials. Cem. Concr. Res. 124, 105806.
Neumann, A., Petit, S., Hofstetter, T.B., 2011. Evaluation of redox-active iron sites in smectites using middle and near infrared spectroscopy. Geochim. Cosmochim. Ac. 75, 2336–2355.
Ortaboy, S., Li, J.Q., Geng, G.Q., Myers, R.J., Monteiro, P.J.M., Maboudian, R., Carraro, C., 2017. Effects of CO2 and temperature on the structure and chemistry of C-(A-)S-H investigated by Raman spectroscopy. Rsc Adv. 7, 48925–48933.
Papadakis, V.G., Antiohos, S., Tsimas, S., 2002. Supplementary cementing materials in concrete - Part II: A fundamental estimation of the efficiency factor. Cem. Concr. Res. 32, 1533–1538.
Pokorný, J., Zaleska, M., Pavlikova, M., Pavlik, Z., 2019. Properties of fine-grained concrete with admixture of diatomite powder. In: IOP Conference Series: Materials Science and Engineering. IOP Publishing, 022045.
Rahhal, V., Talero, R., 2005. Early hydration of Portland cement with crystalline mineral additions. Cem. Concr. Res. 35, 1285–1291.
Rahhal, V., Talero, R., 2009. Calorimetry of Portland cement with silica fume, diatomite and quartz additions. Constr. Build. Mater. 23, 3367–3374.
Rajkumar, R., Yaakob, Z., Takriff, M.S., 2014. Potential of the micro and macro algae for biofuel production: a brief review. Bioresources 9, 1606–1633.
Rao, G.A., 2001. Long-term drying shrinkage of mortar - influence of silica fume and size of fine aggregate. Cem. Concr. Res. 31, 171–175.
Richardson, I.G., 1999. The nature of C-S-H in hardened cements. Cem. Concr. Res. 29, 1131–1147.
Rodriguez, E.T., Richardson, I.G., Black, L., Boehm-Courjault, E., Nonat, A., Skibsted, J., 2015. Composition, silicate anion structure and morphology of calcium silicate hydrates (C-S-H) synthesised by silica-lime reaction and by controlled hydration of tricalcium silicate (C3S). Adv. Appl. Ceram. 114, 362–371.
Rossen, J.E., Lothenbach, B., Scrivener, K.L., 2015. Composition of C-S-H in pastes with increasing levels of silica fume addition. Cem. Concr. Res. 75, 14–22.
Scrivener, K., Snellings, R., Lothenbach, B., 2016. A Practical Guide to Microstructural Analysis of Cementitious Materials. Crc Press Boca Raton.
Sivasundaram, V., Bilodeau, A., Malhotra, V.M., 1995. Effect of curing conditions on high-volume fly ash concrete made with ASTM type I and III cements and silica fume. Amer. Conc. I 154, 509–530.
Snellings, R., Mertens, G., Elsen, J., 2012. Supplementary cementitious materials. Rev. Mineral. Geochem. 74, 211–278.
South, W., 2009. A study of the compressive strength and drying shrinkage of cementitious binders prepared using natural pozzolans. University of Wollongong, Wollongong, Australia.
Sprynskyy, M., Kovalchuk, I., Buszewski, B., 2010. The separation of uranium ions by natural and modified diatomite from aqueous solution. J. Hazard Mater. 181, 700–707.
Tagnit-Hamou, A., Petrov, N., Luke, K., 2003. Properties of concrete containing diatomaceous earth. Aci. Mater. J. 100, 73–78.
Tang, L.P., Nilsson, L.O., 1993. Chloride binding-capacity and binding isotherms of Opc pastes and mortars. Cem. Concr. Res. 23, 247–253.
Taylor, H.F., 1990. Cement Chemistry. Academic press London.
Wang, J.K., Seibert, M., 2017. Prospects for commercial production of diatoms. Biotechnol. Biofuels 10.
Wei, H., He, Q., Jiao, Y., Chen, J., Hu, M., 2016. Evaluation of anti-icing performance for crumb rubber and diatomite compound modified asphalt mixture. Constr. Build. Mater. 107, 109–116.

Wu, L., Ju, X., Liu, M., Guan, L., Ma, Y., Li, M., 2020. Influences of multiple factors on the chloride diffusivity of the interfacial transition zone in concrete composites. Compos. Part B 199, 108236.

Xu, S., Wang, J., Ma, Q., Zhao, X., Zhang, T., 2014. Study on the lightweight hydraulic mortars designed by the use of diatomite as partial replacement of natural hydraulic lime and masonry waste as aggregate. Constr. Build. Mater. 73, 33–40.

Yang, L., Shi, C., Wu, Z., 2019. Mitigation techniques for autogenous shrinkage of ultra-high-performance concrete–a review. Compos. Part B 178, 107456.